# GRAVITY WAVE ENERGETICS DETERMINED FROM COINCIDENT SPACE-BASED AND GROUND-BASED OBSERVATIONS OF AIRGLOW EMISSIONS

# FINAL REPORT

**Grant number:** NGT5-50094 (originally NGT-51641)

**Commencement date:** 1 July 1996 **Period covered in this report:** 1 July 1996 to 31 December 1999

## 1.0 PROGRESS

### 1.1 Academic Progress

The following milestones were achieved during the covered period for this report:

- M.S. in Atmospheric Sciences received in May 1997
- Ph.D. Qualifying Exam passed in May 1999

Completion of the Ph.D. degree in Atmospheric Sciences, and graduation is anticipated by December 2000.

### 1.2 Research Progress

Significant progress was made toward the goals of this proposal in a number of areas during the covered period. Section 5.1 contains a copy of the originally proposed schedule. The tasks listed below have been accomplished:

- Construction of space-based observing geometry gravity wave model

This model has been described in detail in the paper accompanying this report (Section 5.2). It can simulate the observing geometry of both ground-based, and orbital instruments allowing comparisons to be made between them.

- Comparisons of relative emission intensity, temperatures, and Krassovsky's ratio for space- and ground-based observing geometries

These quantities are used in gravity wave literature to describe the effects of the waves on the airglow. See attached paper (Section 5.2).

- *Rejection of Bates* [1992], *and Copeland* [1994] *chemistries for gravity wave modeling purposes*

Excessive $O_2(A'^3\Delta)$ production led to overproduction of $O_2$ ($b^1\Sigma$), the state responsible for the emission of $O_2$ Atmospheric band. Attempts were made to correct for this behavior, but could not adequately compensate for this.

- Rejection of MSX dataset due to lack of coincident data, and resolution necessary to characterize the waves

A careful search to identify coincident data revealed only four instances, with only one of those providing usable data. Two high latitude overpasses and were contaminated by auroral emissions. Of the remaining two mid-latitude coincidences, one overflight was obscured by cloud, leaving only one ten minute segment of usable data. Aside from the statistical difficulties involved in comparing measurements taken in this short period, the instrument lacks the necessary resolution to determine the vertical wavelength of the gravity wave. This means that the wave cannot be uniquely characterized from space with this dataset. Since no observed wave can be uniquely identified, model comparisons are not possible.

# 2.0 PUBLICATIONS AND PRESENTATIONS

## 2.1 Conferences and Workshops

- CEDAR Conference (1996 - 1999)
- Leko, J., Modeling Gravity Wave Affected Airglow Emissions from an Orbital Vantage, Invited presentation given at the 1999 CEDAR meeting, Boulder, CO.
- Leko, J. and M.P. Hickey, A model for transforming ground-based observations of MLT gravity waves to orbiting platforms, Poster presentation given at the 1997 TIMED/CEDAR Workshop, Ellicott City, MD.
- 1997 Fall American Geophysical Union Conference
- 1997 NASA Goddard Space Flight Center High Performance/Computational Physics Summer School

## 2.2 Publications

The following publication is currently being edited for submission to "Geochemistry, Geophysics, and Geosystems: An electronic journal of the Earth Sciences," a new joint-venture web-based journal (http://www-g-cubed.org). A copy of the article text is included in Section 5.2 of the appendix.

- Comparison of simulated gravity wave-driven mesospheric airglow fluctuations observed from the ground and space

Another article based on the momentum and energy deposition work proposed will be drafted for submission pending the completion of the task.

# 3.0 WORK REMAINING

Due to unforeseen difficulties which slowed progress during 1996 and 1997, and the departure of Dr. M. Hickey from the University of Alabama in Huntsville for Clemson University in South Carolina, work has not proceeded as originally scheduled. Dr. Hickey served as the research advisor for this project up to that point. Dr. P. Richards volunteered to continue assisting me with the proposed work, and since the termination of the GSRP in December, has graciously provided support. The momentum and energy flux determinations have been delayed (see Originally Proposed Schedule, Section 5.1). Presently, implementation of the pertinent computer code sections remain. Comparison and analysis of the ground-based model results to published observations will follow. Once completed, results of this work are planned for publication as part of the Ph.D. dissertation as well as in a peer-reviewed journal.

# 4.0 REFERENCES

Bates, D.R., Nightglow emissions from oxygen in the lower thermosphere, *Planet. Space Sci.*, **40**, 211, 1992.

Copeland, R., Laser double resonance study of collisional removal of with $O_2$, *J. Chem. Phys.*, **100**, 744, 1994.

# 5.0 APPENDIX

## 5.1 Originally Proposed Schedule

Year 1

- refinement and continued development of ground- and space-based WKB gravity wave model (***completed***)
- application of various published chemistries to model (***completed***)
- create computer code to calculate energy deposition rates versus altitude (*ongoing*)

- begin acquisition of coordinated MSX data (***completed***)
- begin analysis of ATLAS-1 ISO data (*superseded by MSX dataset due to lack of coincident data*)
- comparison of WKB and full wave model solutions (*not germane to project*)

Year 2

- continue analysis of ATLAS-1 ISO data (*superseded by MSX dataset due to lack of coincident data*)
- begin analysis MSX and ground-based data (***completed***)
- calculate energy deposition rates (*ongoing*)
- comparison of WKB and full wave model solutions (*not germane to project*)

Year 3

- continue MSX and ground-based data analysis (*insufficient data*)
- calculate energy deposition rates (*ongoing*)

## 5.2 In-process publication

# Comparison of simulated gravity wave-driven mesospheric airglow fluctuations observed from the ground and space

J.J. Leko

Atmospheric Sciences Department and Center for Space Plasma and Aeronomic Research, The University of Alabama in Huntsville

M.P. Hickey

Department of Physics and Astronomy, Clemson University, SC

P.G. Richards

Computer Science Department and Center for Space Plasma and Aeronomic Research, The University of Alabama in Huntsville

**Abstract.** Using a theoretical model of gravity wave perturbation of the mesospheric airglow, we compare the expected observations from ground-based and space-based perspectives. $O_2$ Atmospheric (0-1) nightglow emissions are used to illustrate this comparison, and discuss the implications of the ground-based to orbit transformation. The results obtained for the space-based viewing geometry are compared with those obtained for a ground-based viewing geometry for a wide range of gravity wave periods and for horizontal wavelengths of 200, 500, and 1000 km. Additionally, results for the space-based viewing geometry are obtained for several different tangent ray heights varying from well below to above the $O_2$ Atmospheric emission layer. The two different viewing geometries produce nearly the same result for long period waves for tangent ray heights that lie well below the emission layer peak. Results also show that the magnitudes of the relative temperature and intensity fluctuations for space-based observations behave similarly to those for ground-based observations. This work provides an upper limit on Krassovsky's ratio for satellite observations, and shows that orbital observations of wave-induced nightglow fluctuations should be no more difficult to observe than measurements from the ground.

## Introduction

Ground-based observations of upper atmospheric gravity waves have been made by a number of methods for over 30 years [e.g., *Munro*, 1948, 1950, 1953, 1958; *Witt*, 1962; *Krassovsky*, 1972; *Noxon*, 1978; *Hatfield*, 1981; *Hamwey*, 1985; *Gardner*, 1989; *Zhang et al.*, 1992a, b; *Gardner and Taylor*, 1998]. These remote observations are possible because the waves disturb both the thermal, and chemical properties of the regions they traverse. This provides an excellent opportunity to probe the atmosphere above a finite number of points on the Earth. However, as global circulation models (e.g. NCAR's TIMEGCM) become more refined, a need exists for a broader set of observations made on regional and global scales. Satellites provide one method for taking these measurements.

Within the last decade, satellites have detected gravity waves through their effects on airglow [e.g., *Swenson et al.*, 1989; *Ross et al.*, 1992; *Mende et al.*, 1994; *Hays et al.*, 1994; *Armstrong et al.*, 1995; *Dewan et al.*, 1998]. Although the data gathered from these operations cannot completely characterize the waves, one can envision a time in the future when this capability will exist. To prepare for this, and to compare ground- and space-based observations, modeling will be required. This paper presents a model for interpreting space-based data using the $O_2$ Atmospheric (0-1) emission as an example. Results for several gravity wave periods with horizontal wavelengths of 200, 500, and

1000 km are examined, and compared with those from a ground-based perspective. Comparisons use Krassovsky's ratio [*Krassovsky*, 1972], defined as:

$$\int \eta dz = \frac{(\int I' dz)/(\int \bar{I} dz)}{(\int T_I' dz)/(\int \overline{T}_I dz)} \tag{1}$$

which provides a measure of the effect gravity waves have on a given region of the atmosphere at a particular time.Other mesopause region emissions can be generalized from these results [*Schubert et al.*, 1999].

## Model

This work adapts the model of *Hickey et al.* [1993], which uses linearized gravity wave theory in an Eulerian reference frame, to a space-based perspective. Upper and lower boundaries are set well outside the emission layer to circumvent fluctuations encountered when parcels travel into and out of this region, a situation termed "edge effects." The *Garcia and Solomon* [1985] model, in polynomial form, provides the mean state [O], [M] ($M = O_2 + N_2$), temperature, and eddy diffusion profiles which are shown in Figure 1. This model yields an atomic oxygen density peak at 90 km with a FWHM layer thickness of approximately 10 km. The $O_2$ density is set as 21% of [M].

The $O_2$ Atmospheric (0-1) nightglow ($\lambda \geq 8645$Å) intensity is directly proportional to the number density of emitters so that the relative intensity fluctuation is given by $I'/\bar{I} = n'/\bar{n}$. Vertically integrated ground-based airglow observations provide a combination of the mean and perturbed emission intensities, $\int I dz = (\int \bar{I} dz + \int I' dz)$ (where $I$ is the emission intensity, $z$ is the vertical coordinate integrated through the emission region, and $I'$ the perturbation of the background state, $\bar{I}$) and, intensity-weighted temperature data, $\int T_I dz = (\int T_I' dz + \int \overline{T}_I dz)$ (where $\int T_I dz = (\int TI dz)/(\int I dz)$) [*Schubert and Walterscheid*, 1988].

The gravity wave perturbed temperature at an altitude $z$, and horizontal displacement $x$ is given by

$$T'(z) = T'_{75} e^{\frac{z-75}{2H}} e^{i[\omega t - k_x x - k_z(z-75)]} \tag{2}$$

where $T'_{75}$ is the temperature at 75 km, the lower boundary of the model. $H$ is the scale height, $\omega$ the real gravity wave frequency, and $k_x$ and $k_z$ are the horizontal and vertical wavenumbers, respectively. The diffusion of heat and momentum due to eddy processes leads to wave dissipation and provides the imaginary part of $k_z$ in this model.

The minor species concentration for each constituent is computed through the linearized continuity equation:

$$i\omega n' = P' - L' - w' \frac{\partial}{\partial z}\bar{n} - \bar{n}\nabla \bullet v' \tag{3}$$

Here $n'$ is the perturbed $[O_2(b^1\Sigma_g^+)]$ density about its mean value $\bar{n}$, $P'$ and $L'$ are the perturbed chemical production and loss terms respectively, $w'$ is the perturbed vertical velocity, $\nabla \bullet v'$ is the perturbed vertical velocity divergence due to the gravity wave, and $\omega$ is the gravity wave angular frequency. Perturbation quantities are assumed to vary according to $exp\ i(\omega t - k_x x)$. The production and loss terms in (3) require specification of the $O_2$ Atmospheric (0-1)

chemistry, which is given in Table 1. Altitude profiles for the $[O_2(c^1\Sigma_u^-)]$ and $[O_2(b^1\Sigma_g^+)]$ are shown in Figure 2, with

Table 1: Chemical model of the $O_2$ Atmospheric (0-1) nightglow (after *Hickey et al.*, [1993])

| Reaction | Rate Reaction* |
|---|---|
| $O + O + M \rightarrow O_2 + M$ | $k_1 = 4.7 \times 10^{-45}(300/\bar{T})^2$ |
| $O + O + M \rightarrow O_2(b^1\Sigma_g^+) + M$ | $k = ek_1$, e= 0.11 |
| $O + O + M \rightarrow O_2(c^1\Sigma_u^-) + M$ | $k = \xi k_1$, $\xi$= 0.8 |
| $O_2(c^1\Sigma_u^-) + O_2 \rightarrow O_2(b^1\Sigma_g^+) + O_2$ | $k_2 = 5.0 \times 10^{-19}$ |
| $O_2(c^1\Sigma_u^-) + O \rightarrow O_2(b^1\Sigma_g^+) + O$ | $k_3 = 3.0 \times 10^{-17}$ |
| $O_2(b^1\Sigma_g^+) + O \rightarrow O_2 + O$ | $k_4 = 8.0 \times 10^{-20}$ |
| $O_2(b^1\Sigma_g^+) + N_2 \rightarrow O_2 + N_2$ | $k_5 = 2.2 \times 10^{-21}$ |
| $O_2(b^1\Sigma_g^+) + O_2 \rightarrow 2O_2$ | $k_6 = 4.0 \times 10^{-23}$ |
| $O_2(c^1\Sigma_u^-) \rightarrow O_2 + h\nu$ (Herzberg II bands) | $A_1 = 2.0 \times 10^{-2}$ |
| $O_2(b^1\Sigma_g^+) \rightarrow O_2 + h\nu$ ($O_2$ Atmospheric bands) | $A_2 = 8.3 \times 10^{-2}$ |

*Units are $s^{-1}$, $m^{-3}\ s^{-1}$, and $m^{-6}\ s^{-1}$ for unimolecular, bimolecular, and termolecular, respectively.

the latter calculated through a combination of both Barth (two-stage population using the $[O_2(c^1\Sigma_u^-)]$ state as the intermediary) and Chapman (direct population) processes.

The solution to (3) for the minor species depends on the complex dynamical factors $f_1$, $f_2$, and $f_3$ given by:

$$\nabla \bullet v' = f_1 \frac{T'}{\bar{T}} \tag{4}$$

$$w' = f_2 \frac{T'}{\bar{T}} \tag{5}$$

$$n'(M) = f_3 \bar{n}(M) \frac{T'}{\bar{T}} \tag{6}$$

which relate the velocity divergence, the vertical velocity, and the major gas density perturbation to the temperature perturbation [*Walterscheid et al.*, 1987].

The ground-based viewing geometry is transformed to limb-viewing geometry through a phase shift technique as illustrated in Figure 3. This shows a gravity wave, $\psi'_0(z)$, whose fluctuations at a given time depend only on altitude, $z$, making an angle $\theta = 0^o$ with the zenith. If one assumes without loss of generality that the wave can occur at any angle from the zenith, the necessary foundation is laid for space-based simulations.

The transformation proceeds from planar (ground-based) to cylindrical (orbital) geometry by replacing the displacement $x$ in the planar system with the arc length $s = (R_E + z) \bullet \theta$ in the cylindrical system, where $R_E$ is the Earth's radius, and $z$ is altitude. The wave parameters at point B on the gravity wave, can be transformed to positions A, or C with the expression $\psi'(\theta, z) = \psi'(0, z)e^{ik_x s}$. In Figure 3, points A, B, and C are all at the same altitude, $z$, but their respective displacements are $s$, 0, and -$s$. Integration of the fluctuation quantities is performed across this slant path OAC, with each of the points of interest computed using this transform.

Using symmetry, approximations may be made to reduce the computational requirements of the calculations. It is recognized that the perturbations are related to one another by

$$\psi'_B(0,z)e^{ik_x s} = \psi'_A(\theta,z) = \psi'_C(-\theta,z)\,. \tag{7}$$

Except for the tangent ray point itself, for every perturbation at position $(\theta, z)$ that contributes to the integral there will be a corresponding contribution for the perturbation at position $(-\theta, z)$. Using (7), the sum of the perturbations at altitude $z$ is equal to $2\psi'_B(0,z)\cos(k_x s)$. Note that although the perturbations at A and C are each represented as a complex number multiplied by the perturbation at B, their sum is a purely real number multiplied by the perturbation at B.

Assuming the tangent ray path, identified by the line passing through points O, A, and C, is normal to the gravity wave phase fronts, and that the mean atmosphere depends only on altitude, the perturbations at a fixed time will depend only on position $(\theta, z)$. The justification for modeling gravity waves as planar waves on a spherical Earth is given by *Francis* [1972]. Since the model geometry requires the tangent ray height (TRH) as an input, analysis of observations other than limb viewing from space are not possible. Another shortcoming of this approach is that dissipation along the slant path is not considered in this model.

## Results

We compare perturbed to mean intensity and temperature ratios for both ground, and space geometries. These component parts provide a window on the behavior of the Krassovsky's ratio function. Results are presented for waves with horizontal wavelengths of 200, 500, and 1000 km since they are observable from both ground and orbit [e.g., *Swenson et al.*, 1992; *Mende et al.*, 1994]. For each horizontal wavelength ($\lambda_H$) value, 50 waves are simulated having horizontal phase speeds ranging from 2 to 2500 m $s^{-1}$. A non-isothermal atmosphere is used in all simulations.

Figure 4 shows the perturbed to mean intensity ratio for ground, and space geometries for several $\lambda_H$. There are two features of note. First, all $\lambda_H$ shown, both ground and space cases, exhibit a decrease in $|\langle I'\rangle|/\langle \bar{I}\rangle$ as wave period increases. This is due to the decrease in vertical wavelength, $\lambda_V$, which accompanies increasing wave period resulting in destructive interference. As $\lambda_V$ decreases to an integer multiple of the emission layer thickness, phase cancellation occurs which decreases the integrated brightness of the emission [*Hines and Tarasick*, 1987; *Schubert and Walterscheid*, 1988; *Schubert et al.*, 1991]. The second result of interest in this figure are the differences between the ground and space results at each $\lambda_H$. While long and intermediate $\lambda_H$ principally mirror each other with minor digressions, this is not true for the 200 km case. Here, space and ground are clearly distinct with the orbital case having the larger magnitude. We attribute this to the increased length of the limb viewing slant path, with our rationale as follows. The mean emission intensity observed from the ground will always be less than that observed from a limb viewing orbital position. However, this would cause the quantity, $|\langle I'\rangle|/\langle \bar{I}\rangle$, for space to be less than that for ground. The key then must lie with the perturbed intensity, which much be greater in the space case then for ground observations. This is possible since gravity waves will produce a more pronounced effect on the limb view than on the ground-based slant path, hence increasing the space-based perturbed intensity. This may not, however, hold strictly true for actual space-based observations since the gravity wave may only affect a smaller portion of the slant path. This would decrease the perturbed intensity, and narrow the difference between the ground and orbital cases possibly even reversing the two results.

The perturbed to mean temperature ratio in Figure 5 exhibits many of the same features discussed above. For all $\lambda_H$, $|\langle T'\rangle|/\langle \bar{T}\rangle$ decreases with increasing wave period. Space and ground results generally are in good agreement for long and medium $\lambda_H$ waves, but are distinct in the 200 km case. $|\langle T'\rangle|/\langle \bar{T}\rangle$ composes the denominator of Krassovsky's ratio. It should be noted that while the temperature and intensity ratios behave similarly, they do not necessarily vary in phase with one another. Temperature is a quantity which is directly transported by the gravity wave, while intensity

relies on several factors (i.e., metastable state lifetimes, species densities, reactions rates, etc.) which may delay wave influence.

Having discussed the components of Krassovsky's ratio, we now examine its magnitude, $|\eta|$, for both orbital and ground cases. Figure 6 shows modeled ground and space results of Krassovsky's ratio for three horizontal wavelengths. The modeled ground-based $|\eta|$ values have larger magnitudes than the space-based component for the same conditions. Orbital simulations are modeled at a TRH of 75 km, which allows the slant path to fully scan through the emission region. Other TRHs will be shown in subsequent plots. The division separating evanescent waves from internal gravity waves occurs at progressively longer periods as the horizontal wavelength increases. It is apparent from this plot that waves of shorter horizontal wavelength produce larger $|\eta|$ values than do larger horizontal wavelength waves. This is attributed to the near-zero magnitude of the relative temperature fluctuation.

Figure 7 shows both ground- and space-based Krassovsky's ratios for a 200 km horizontal wavelength wave at different TRHs. The ground result (solid line) agrees well with *Hickey et al.* [1993], and is most closely approximated by the orbital results modeled from 75 and 80 km TRHs. Comparisons of the Krassovsky's ratio ground-based results to those of *Hickey et al.* [1993] should be made with the Spring, 18° latitude results from that paper. There are minor differences owing to differences in the background profiles. The agreement between space and ground is best at long periods, and low TRHs. It is worst at the emission peak. Omission of the region below the emission peak (~ 10 km in this case) ignores significant interference effects which can enhance or detract from $|\eta|$.

Figure 8 is similar to Figure 7, but for $\lambda_H$ of 1000 km. In this figure, the ground result agrees quite well with those for TRHs of 75, and 80 km for long periods. Interference effects are the cause. $\lambda_V$, for long periods and 200 km $\lambda_H$ for instance, is approximately half of the emission region extent. This indicates that within one vertical wavelength, both emission enhancement and cancellation occur, resulting in no overall effect on the emission intensity. Whereas for long periods and a 1000 km $\lambda_H$, $\lambda_V$ occupies at least three-quarters of the emission region at a given time causing either constructive, or destructive interference of the emission.

## Discussion

Many are familiar with the results and techniques used to measure the mean intensity of an emission from orbit. In this situation, the brightest intensities are recorded in a region immediately surrounding the peak species density. Our simulations reveal that space-based determinations of Krassovsky's ratio for large horizontal wavelength gravity waves are expected to agree with their ground-based counterparts only for TRHs that lie well below the peak of the observed nightglow emission. For greater TRHs, there is little agreement between ground- and space-based values of Krassovsky's ratio at almost all wave periods save for a few points. Agreement becomes progressively worse as the horizontal wavelength is decreased.

The wave model assumes that the atmosphere is cylindrically homogeneous (i.e., that it does not depend on azimuth). For a TRH of 75 km and an upper boundary of 130 km, this is equivalent to assuming that the atmosphere is homogeneous over a horizontal extent of about 1700 km. At low latitudes this appears to be a reasonable assumption: 1700 km corresponds to a small change in latitude or longitude and is about 4% of the Earth's circumference. At higher latitudes, the homogeneous assumption will not be valid, and mean state (including tidal) variations may need to be accounted for in the determination of the background atmosphere.

We have also assumed an idealized viewing geometry with the slant path normal to the gravity wave phase fronts for the space-based simulations. In general, this will not be the case, and values of Krassovsky's ratio under such conditions may be different from those calculated here. Under such circumstances the azimuth of wave propagation with respect to the viewing direction would be required in order to correctly simulate such observations, and a spherical geometry would replace the cylindrical geometry used here.

We have shown that for a 75 km TRH the magnitude of the space-based relative intensity fluctuation exceeds its ground-based counterpart by as much as a factor of 5, for short horizontal wavelengths and gravity wave periods. This

implies that wave-driven nightglow emission fluctuations should be no more difficult to detect from space than from the ground for a particular emission. Since shorter horizontal wavelength waves have smaller relative intensity fluctuations than the longer wavelength waves, the 200 km $\lambda_H$ results are the worst case.

It is regrettably not possible to compare these simulations with orbital observations at this point. Although space-based instruments such as those aboard the MSX satellite [*Dewan et al.*, 1998; *Romick and Yee*, personal communication], and ATLAS-1 AEPI [e.g.,*Swenson et al.*, 1992] have recorded gravity wave activity, data required to completely characterize the gravity waves are unavailable. To define a gravity wave from space two pieces of information are required: the horizontal, and vertical wavelengths. Determination of the gravity wave period, the third basic piece of information about the wave, is not easily achieved from space. From the ground, the wave period is recorded at a point by measuring the time required for a wavelength to pass. In space however, the spacecraft travels through (or by) the wave swiftly making the wave appear to stand still in comparison. This precludes measurement of the period from orbit.

## Conclusion

A technique is presented for a simple transformation which may be applied to existing gravity wave-nightglow interaction models with ground-based viewing geometry to simulate orbital observations. $O_2$ Atmospheric (0-1) nightglow emissions are used to illustrate this method, and discuss the implications of the transformation. The results obtained for the space-based viewing geometry are compared with those for a ground-based viewing geometry for a wide range of gravity wave periods and for horizontal wavelengths of 200, 500, and 1000 km.

Unlike techniques to observe the mean emission intensity, the best agreement between space and ground $|\eta|$ simulations occurred for TRHs well below the emission layer peak. This is useful for obtaining limb viewing observations of gravity waves where the intuitive plan might be to scan the slant path through the peak emission altitude. Results also showed that for TRHs below the emission peak the relative intensity and temperature fluctuations for orbital simulations behave similarly to ground-based simulations exhibiting a magnitude decrease as the wave period was increased. Finally, the best agreement between orbital and ground-based simulations for Krassovsky's ratio occurs for large horizontal wavelengths.

**Acknowledgments.** This research was supported by NSF grant ATM-94O2434, and NASA grants NGT-51641 and NGT5-50094 to the University of Alabama in Huntsville.

## References

Armstrong, W. T., U-P. Hoppe, G. G. Shepherd, and B. Solheim, Observations of gravity wave structure in $O_2$ (0-0) airglow measurements with the UARS-WINDI imager, *EOS Trans.*, 76, no. 46, F73, 1995.

Dewan, E.M., R.H. Picard, R.R. O'Neil, H.A. Gardiner, J. Gibson, J.D. Mill, E. Richards, M. Kendra, W.O. Gallery, MSX satellite observations of thunderstorm-generated gravity waves in midwave infrared images of the upper stratosphere, *Geophys. Res. Lett., 25*, 939-942, 1998.

Francis, S. H., Propagation of internal acoustic-gravity waves around a spherical earth, *J. Geophys. Res.*, 77, 4221, 1972.

Garcia, R.R., and S. Solomon, The effects of breaking gravity waves on the dynamics and chemical composition of the mesosphere and lower thermosphere, *J. Geophys. Res., 90*, 3850, 1985.

Gardner, C.S., Sodium resonance fluorescence applications in atmospheric science and astronomy, *Proc. IEEE, 77(3)*, 408-418, 1989.

Gardner, C.S., and M.J. Taylor, Observational limits for lidar, radar, and airglow imager measurements of gravity wave parameters, *J. Geophys. Res, 103*, 6427-6439, 1998

Hamwey, R.M., A spectrophotometric study of hydroxyl emissions from a high latitude winter mesopause, M.S. thesis, Univ. of Alaska, Fairbanks,

1985.

Hatfield, R., T.F. Tuan, and S.M. Silverman, On the effects of atmospheric gravity waves on profiles of H, $O_3$, and OH emission, *J. Geophys. Res., 86*, 2429-2437, 1981.

Hays, P. B., G. Fall, B. Solheim, and G. G. Shepherd, Observing atmospheric waves from the UARS spacecraft, EOS Trans., 75, no. 44, 111, 1994.

Hickey, M. P., G. Schubert and R. L. Walterscheid, Gravity wave-driven fluctuations in the $O_2$ Atmospheric (0-1) nightglow from an extended, dissipative emission region, *J. Geophys. Res., 98*, 13,717, 1993.

Hickey, M.P., Effects of eddy viscosity and thermal conduction and Coriolis force in the dynamics of gravity wave driven fluctuations in the OH nightglow, *J. Geophys. Res., 93*, 4,077, 1988.

Hines, C. 0., and D. W. Tarasick, On the detection and utilization of gravity waves in airglow studies, *Planet. Space Sci., 35*, 851, 1987.

Krassovsky, V.I., Infrasonic variations of OH emission in the upper atmosphere, *Ann. Geophys., 28*, 739, 1972.

Mende, S. B., G. R. Swenson, S. P. Geller, and K. A. Spear, Topside observations of gravity waves, *Geophys. Res. Lett., 21*, 2283, 1994.

Munro, G.H., Short-period changes in the *F* region of the ionosphere, *Nature, 162*, 886, 1948.

Munro, G.H., Travelling disturbances in the ionosphere, *Proc. R. Soc., Ser. A, 202*, 208, 1950.

Munro, G.H., Reflexions from irregularities in the ionosphere, *Proc. R. Soc., Ser. A, 219*, 447, 1953.

Munro, G.H., Travelling ionospheric disturbances in the *F* region, *Aust. J. Phys., 11*, 91, 1958.

Noxon, J. F., Effect of internal gravity waves upon night airglow temperatures, *Geophys. Res. Lett., 5*, 25, 1978.

Ross, M. N., A. B. Christensen, C. I. Meng, and J. F. Carbary, Structure in the uv nightglow observed from low Earth orbit, *Geophys. Res. Lett., 19, 985*, 1992.

Schubert, G., and R.L. Walterscheid, Wave-driven fluctuations in OH nightglow from and extended source region, *J. Geophys. Res., 93*, 9903-9915, 1988.

Schubert, G., R. L. Walterscheid and M. P. Hickey, Gravity wave-driven fluctuations in OH nightglow from an extended, dissipative emission region, *J. Geophys. Res., 96*, 13,869, 1991.

Schubert, G., R.L. Walterscheid, M.P. Hickey, and C.A. Tepley, Observations and interpretation of gravity wave induced fluctuations in the O I (557.7 nm) airglow, *J. Geophys. Res., 104*, 14915-14924, 1999.

Swenson, G. R., S. B. Mende, and E. J. Llewellyn, Imaging observations of lower thermospheric $O(^1S)$ and $O_2$ airglow emissions from STS-9: Implications of height variations, *J. Geophys. Res., 94*, 1417, 1989.

Swenson, G. R., S. B. Mende, and R. Rairden, Observations of airglow structure in the of nadir and limb with AEPI imagers on ATLAS-1, *EOS Trans., 428*, 1992. (SA42A-9)

Walterscheid, R.L., G. Schubert, and J.M. Straus, A dynamical-chemical model of wave-driven fluctuations in the OH nightglow, *J. Geophys. Res., 92*, 1241, 1987.

Witt, G., Height structure, and displacement of noctilucent cloud, *Tellus, 14*, 1, 1962.

Zhang, S.,R.N. Peterson, R.H. Wiens, and G.G. Shepherd, Gravity waves from $O_2$ nightglow during the AIDA '89 Campaign, I, Emission rate/temperature observations, *J. Atmos. Terr. Phys.*, 355, 1992a.

Zhang, S., R.H. Wiens, and G.G. Shepherd, Gravity waves from $O_2$ nightglow during the AIDA '89 Campaign, II, Numerical modeling of the emission rate/temperature ratio, $\eta$, *J. Atmos. Terr. Phys.*, 377, 1992b.

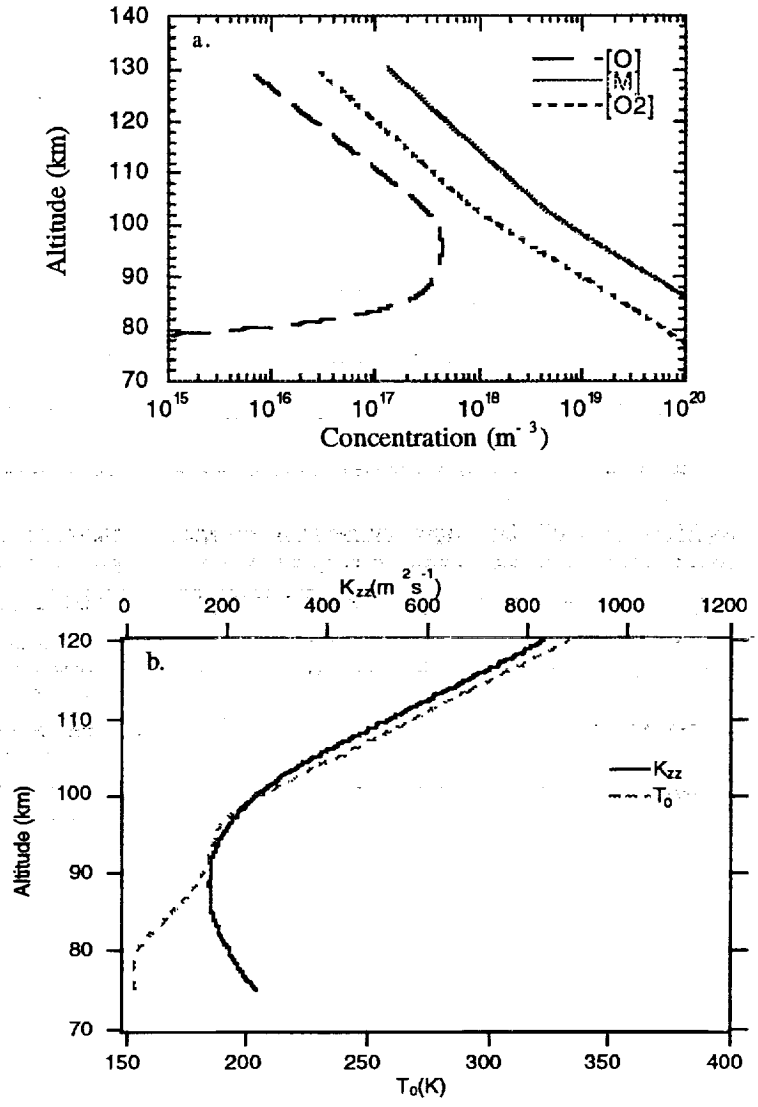


Figure 1. Background a. major gas, atomic and molecular oxygen, b. temperature ($T_0$), and eddy diffusion profiles ($K_{zz}$).

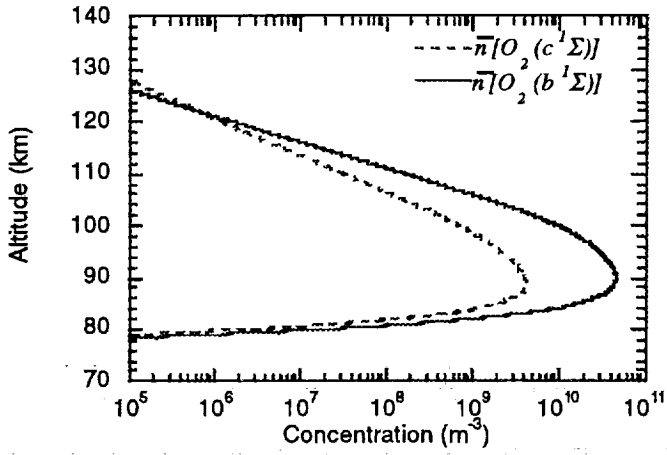


Figure 2. Derived mean $[O_2(c^1\Sigma_u^-)]$ and $[O_2(b^1\Sigma_g^+)]$ with the later calculated through a combination of both Barth (two-stage population) and Chapman (direct population) processes.

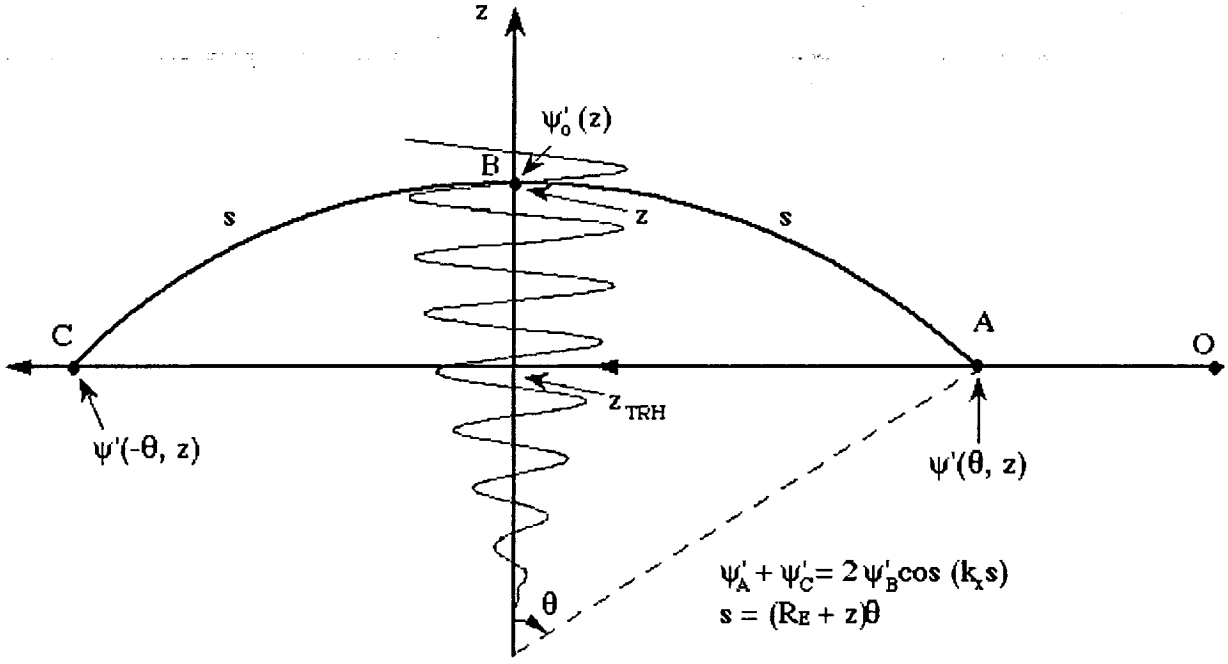


Figure 3. Schematic (not to scale) illustrating the cylindrical geometry wherein points A, B, and C all lie at the same altitude, z, and the line of sight extends from the observer (at O) through points A, C, and the tangent ray point (at height $z_{TRH}$). The arc length, s, and the horizontal wavenumber, $k_x$, are used to define the perturbations at points A and C in terms of the perturbation at point B. Symmetry is used to decrease the number of integration steps by folding the slant path about the TRH line, which gives the factor 2.

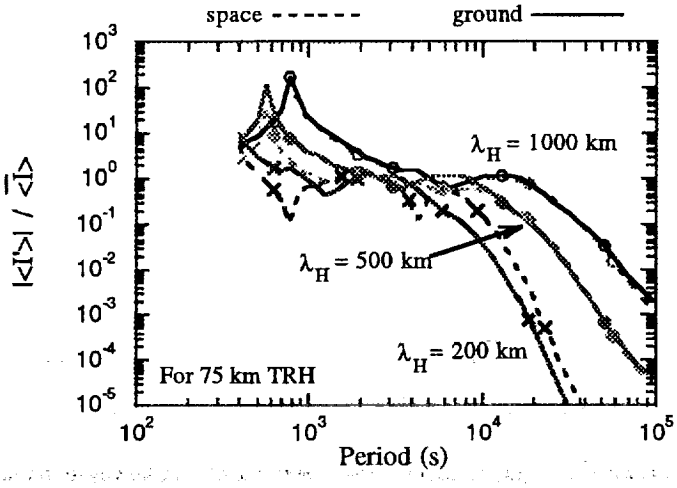


Figure 4. Simulated magnitude of the gravity wave-driven $O_2$ Atmospheric emission relative intensity fluctuation, $|\langle I' \rangle| / \langle \bar{I} \rangle$, as a function of wave period for waves with horizontal wavelengths of 200, 500, and 1000 km, and for both ground-based (solid curves) and space-based (dashed curves) viewing geometries.

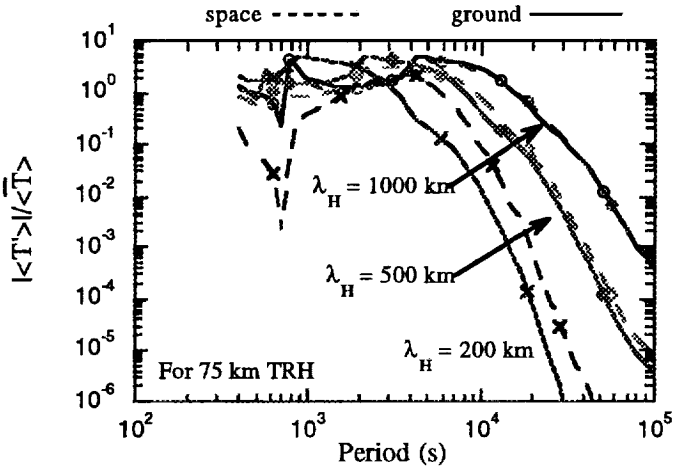


Figure 5. Simulated magnitude of the gravity wave-driven $O_2$ Atmospheric emission relative intensity fluctuation, $|\langle T' \rangle| / \langle \bar{T} \rangle$, as a function of wave period for waves with horizontal wavelengths of 200, 500, and 1000 km, and for both ground-based (solid curves) and space-based (dashed curves) viewing geometries.

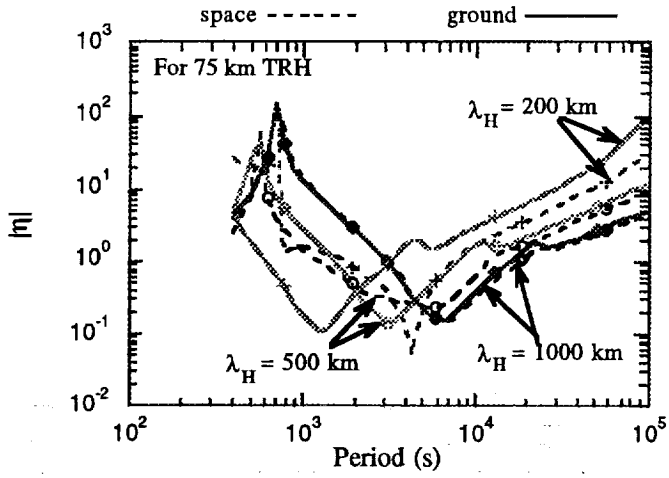


Figure 6. Simulated magnitude of Krassovsky's ratio, $|\eta|$, for the $O_2$ Atmospheric emission as a function of wave period for horizontal wavelengths of 200, 500, and 1000 km. The solid curves represent the simulations for ground-based viewing, while the dashed curves represent the simulations for space-based viewing with a tangent ray height of 75 km.

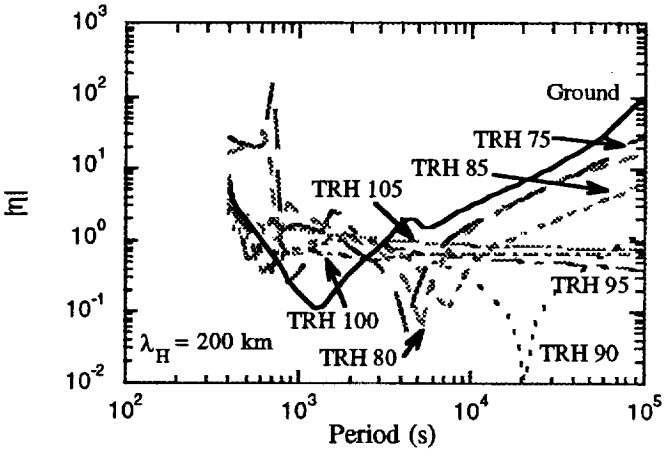


Figure 7. Simulated magnitude of Krassovsky's ratio, $|\eta|$, for the $O_2$ Atmospheric emission as a function of wave period for a horizontal wavelength of 200 km. The solid curves represent the simulations for the ground-based viewing, while the other curves represent the simulations for space-based viewing with various tangent ray heights varying from 75 to 105 km altitude.

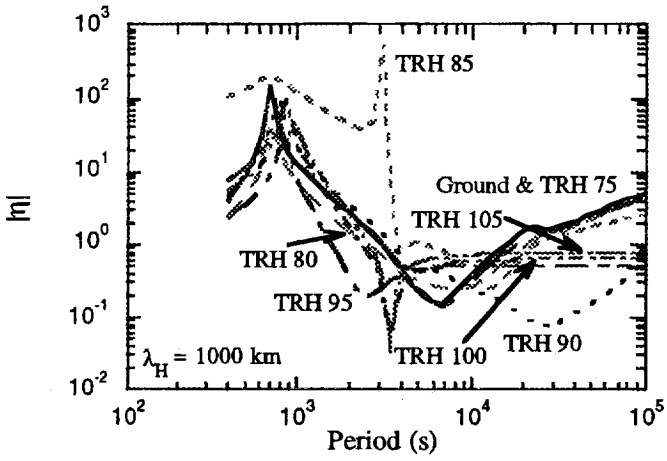


Figure 8. Simulated magnitude of Krassovsky's ratio, $|\eta|$, for the $O_2$ Atmospheric emission as a function of wave period for a horizontal wavelength of 1000 km. The solid curves represent the simulations for the ground-based viewing, while the other curves represent the simulations for space-based viewing with various tangent ray heights varying from 75 to 105 km altitude.